# Computational Study of the Reaction of 1-Methyl-4-amino-1,2,4-triazolium Dicyanamide with NO_2: From Reaction Dynamics to Potential Surfaces, Kinetics and Spectroscopy

Jianbo Liu,*,[†] Wenjing Zhou,[†] Steven D. Chambreau,[‡] and Ghanshyam L. Vaghjiani[§]

[†]Department of Chemistry and Biochemistry, Queens College and the Graduate Center of the City University of New York, 65-30 Kissena Boulevard, Queens, New York 11367, United States

[‡]ERC, Inc., Air Force Research Laboratory, Edwards Air Force Base, California 93524, United States

[§]In-Space Propulsion Branch, Rocket Propulsion Division, Aerospace Systems Directorate, Air Force Research Laboratory, AFRL/RQRS, Edwards Air Force Base, California 93524, United States

S *Supporting Information*

ABSTRACT: Direct dynamics trajectories were calculated at the B3LYP/6-31G(d) level of theory in an attempt to understand the reaction of 1-methyl-4-amino-1,2,4-triazolium dicyanamide (MAT^+DCA^-) with NO_2. The trajectories revealed an extensive intra-ion-pair proton transfer in MAT^+DCA^-. The reaction pathways of the ensuing HDCA (i.e., HNCNCN) and $[MAT^+ - H_{C5}^+]$ (i.e., deprotonated at C5−H of MAT^+) molecules as well as DCA^- with NO_2 were identified. The reaction of NO_2 with HDCA and DCA^- produces $HNC(−ONO)NCN$ and $NCNC(−ONO)N^-$ or $NCNCN−NO_2^-$, respectively, whereas that with $[MAT^+ - H_{C5}^+]$ results in the formation of 5-O-MAT (i.e., 4-amino-2-methyl-2,4-dihydro-3H-1,2,4-triazo-3-one) + NO and $[MAT^+ - H_2^+]$ + HNO_2. Using trajectories for guidance, structures of intermediates, transition states and products, and the corresponding reaction potential surfaces were elucidated at B3LYP/6-311++ G(d,p). Rice−Ramsperger−Kassel−Marcus (RRKM) theory was utilized to calculate the reaction rates and statistical product branching ratios. A comparison of direct dynamics simulations with RRKM modeling results indicate that the reactions of NO_2 with HDCA and DCA^- are nonstatistical. To validate our computational results, infrared and Raman spectra of MAT^+DCA^- and its reaction products with NO_2 were calculated using an ionic liquid solvation model. The calculated spectra reproduced the vibrational frequencies detected in an earlier spectroscopic study of MAT^+DCA^- droplets with NO_2 [Brotton, S. J.; et al. *J. Phys. Chem. Lett.* 2017, 8, 6053].
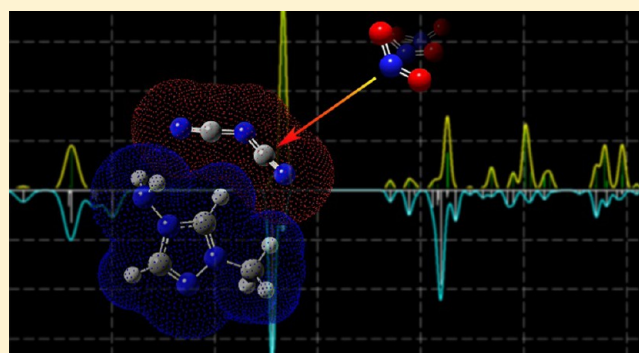
1. INTRODUCTION

Imidazolium- and triazolium-based cations, when paired with the hypergolic dicyanamide anions ($NCNCN^-$, abbreviated as DCA^-),[1−4] are expected to produce lower-vapor-pressure ionic liquids (ILs) with improved hypergolic reactivity, which have short ignition delay time, high stabilities, and favorable physical properties for storage, transportation, loading, and processing. They have therefore become of interest in the aerospace community as green propellant alternatives to the highly toxic, volatile, and sensitive hydrazine (including its derivatives) for rocket propulsion applications.[5,6] To predict the performance of hypergolic ILs and optimize the design of propulsion systems that use IL fuels, it is essential to understand the IL thermal stabilities, oxidation mechanisms, reaction dynamics, and reaction kinetics. We previously reported photoionization mass spectrometric and Fourier transform infrared (FT-IR) spectroscopic studies[7] and molecular dynamics simulations[8] of the thermal decomposition of 1-ethyl-3-methylimidazolium dicyanamide ($EMIM^+DCA^-$) and 1-ethyl-2,3-dimethylimida-

zolium dicyanamide ($EMMIM^+DCA^-$). The combination of experimental and theoretical approaches was able to determine the decomposition products, branching ratios, and underlying reaction kinetics and reaction dynamics of alkylimidazolium-DCA ILs. The commonly used oxidizers for the hypergolic ignition of DCA-containing ILs include nitric acid[9−11] and NO_2;[12,13] in the latter case, the actual thruster involves the dissociation of dinitrogen tetroxide (N_2O_4) to NO_2. Recently, Kaiser et al.[12] investigated the reaction of levitated droplets of 1-methyl-4-amino-1,2,4-triazolium dicyanamide (MAT^+DCA^-) with NO_2 using FT-IR and Raman spectroscopic probes, in which many new vibrational bands were observed in the end-products. Some of the new vibrations were attributed to the formation of a NO_2 adduct of DCA^-, but many others remained unassigned. The present work aims to explore the reaction of

MAT$^+$DCA$^-$ with NO$_2$ theoretically, in an attempt to predict the reaction pathways and products and accordingly deduce the relevant reaction potential energy surfaces (PESs).

For energetic ILs with high internal energy content, cognitive use of chemical intuition to predict reaction pathways may be inadequate and sometimes unreliable. There may exist concerted processes and multiple competing initiation reactions (particularly at high temperatures) that are difficult to predict.[8,14] Once the stored energy in a reacting IL molecule begins to release, the system is controlled by dynamics[15] and does not necessarily follow an intrinsic reaction coordinate (IRC) path (one with the steepest descent path leading from the transition state (TS) to the potential minimum on the PES). The subsequent reaction(s) may be autocatalytic,[16] and nonstatistical reactions may arise from direct collisions, non-IRC paths, or non-Rice−Ramsperger−Kassel−Marcus unimolecular processes.[17,18] An appropriate approach for treating these systems is direct dynamics simulations.[18−27] Direct dynamics trajectories explore multiple minima in the conformational landscape and the reaction PES. The motions of the molecules are directly followed, thus allowing the molecules to show what the preferred pathways are. Since the reaction energy is distributed among vibrational, rotational, and translational modes, it increases the chance of identifying new unexpected reactions.[18,25,27] Moreover, by following the variations in energy and bond lengths along the trajectories, we can identify a reaction instant that corresponds to an activation barrier and use that geometry as an input for calculating the TS.[25,26,28] In direct dynamics simulations, there is no need to develop an analytical PES; instead, energies, force constants, and Hessians are calculated "on the fly". Therefore, this method becomes computationally attractive for large systems.

Direct dynamics simulations were carried out for both primary and secondary reactions in the MAT$^+$DCA$^-$ + NO$_2$ system. Using trajectory results as a guide, PESs for the intra-ion-pair proton transfer (PT) in MAT$^+$DCA$^-$ and for the reactions of NO$_2$ (such as hydrogen transfer, HT) with DCA$^-$ anion, neutral HDCA (i.e., HNCNCN) and [MAT$^+$ − H$_{C5}^+$] were mapped out using density functional theory (DFT). Rice−Ramsperger−Kassel−Marcus (RRKM) theory[29] was then employed to examine whether the reactions followed statistical mechanisms or not. Finally, to validate the computational results, IR and Raman spectra of the theoretically predicted products were calculated and compared with Kaiser et al.'s spectrometric measurements.[12]

2. APPROACHES FOR DYNAMICS SIMULATIONS, KINETICS MODELING, AND SPECTRAL ANALYSIS

Detailed computational methodologies are available in the Supporting Information. Here, only a brief description is given. Trajectories were calculated using the VENUS program[30,31] to set up initial conditions, and the Hessian-based predictor−corrector algorithm[24] was implemented in Gaussian 09[32] to integrate trajectories with the Hessian matrix updated every five steps. The B3LYP/6-31G(d) level of theory was used for the simulations, as it has been used successfully in calculating the energetics of dialkylimidazolium-[33−37] and triazolium-based[2] ILs and the reaction dynamics of EMIM$^+$DCA$^-$ and EMMIM$^+$DCA$^-$.[8] Trajectories were propagated with a step size of 0.25 amu$^{1/2}$ Bohr (corresponding to 0.4 fs). A quadratically convergent self-consistent field (SCF) procedure[32,38] was adopted in those cases when first-order SCF failed to converge. Trajectories of representative collisions were

recalculated at the M06/6-31G(d) level of theory, as the latter was used for the spectral analysis in Kaiser et al.'s work.[12] The M06 trajectories were found to follow similar pathways and revealed similar dynamics as the B3LYP trajectories. All calculations were completed on a Linux computer cluster at Queens College. gOpenMol[39] was used for trajectory visualization. Analyses of individual trajectories and trajectory ensembles were carried out with programs written by us for these purposes, which had automated algorithms to search and sort reaction pathways.

Using trajectory results as a guide, structures of reactants, intermediates, TSs, and products along all of the reaction pathways were optimized at the B3LYP/6-311++G(d,p) level of theory. Cartesian coordinates of these species are provided in the Supporting Information. Reaction PESs were evaluated by the sum of electronic energies, zero point energies (ZPEs), and thermal corrections at 298 K, for which the vibrational frequencies and ZPEs were scaled by a factor of 0.955 and 0.981,[40] respectively. Statistical outcomes of reaction PESs were predicted using the RRKM theory. The RRKM densities of states and rate constants were calculated using a direct count algorithm[41] and the scaled frequencies, energetics, and moments of inertia of the complexes and TSs are determined from the B3LYP/6-311++G(d,p) level of theory calculations.

To simulate reactant and product IR and Raman spectra in a condensed-phase IL environment, important structures were reoptimized using a parameterized SCRF-based SMD[42] method (also known as the generic ionic liquid solvation model, SMD-GIL)[43] and solvent parameters that were consistent with the experiment (vide infra).

3. TRAJECTORY RESULTS AND REACTION PESS

3.1. MAT$^+$DCA$^-$ + NO$_2$. Prior to the trajectory simulations, the conformations of MAT$^+$DCA$^-$ had been screened. In the B3LYP-calculated lowest-energy conformer of MAT$^+$DCA$^-$, the DCA$^-$ moiety stays above the triazolium ring with its two terminal N-atoms pointing to the CH$_3$ and NH$_2$ groups of MAT$^+$, respectively. It is to be noted that MAT$^+$DCA$^-$ was vigorously excited in the trajectories due to collisional activation and thermal excitation. Consequently, albeit a global minimum structure of MAT$^+$DCA$^-$ was being used as the starting reactant in the simulations, the trajectories have actually explored all energetically accessible structures along the trajectory integration, and a mix of various conformers contributed to the reactions simultaneously. This represents the true nature of direct dynamics: that is to explore reaction pathways in an unbiased manner.

We first simulated the reaction of NO$_2$ with an intact MAT$^+$DCA$^-$ ion pair at room temperature and two different E_{col} (0.1 and 0.5 eV) values. Trajectories were started with randomly oriented reactants at a center-of-mass separation of 9.0 Å, and reactants vibrational and rotational energies were sampled from Boltzmann distributions (see the details in the Supporting Information). One hundred trajectories were calculated for each of the two collision conditions. But neither of the two conditions led to any reactions within the trajectory integration time (∼1 ps). The lack of reactions in the room-temperature simulations was not really surprising, since the reaction time in the experiments was found to be long.[12,13] To enhance the reaction probability in the trajectories, we needed to run simulations at higher temperatures. To find a reasonable temperature range for accelerating the reactions but not overwhelmingly decomposing the reactants, we completed a series of tests at the HF/6-31G(d)

Table 1. Trajectory Reaction Probabilities (%) for MAT$^+$DCA$^-$ + NO$_2$ at Various Conditions^a

temperature (K)	300		1000	2000	3000	4000	5000
E_{col} (eV)	0.1	0.5	0.5	0.5	0.5	0.1	0.1
PT1: $[MAT^+ - H_{C5}^+]$ + HDCA	0	0	20 ± 4	10 ± 3	35 ± 5	24 ± 4	29 ± 4
PT2: $[MAT^+ - H_{C5}^+]$ + HN(CN)$_2$	0	0	0	5 ± 2	10 ± 3	13 ± 3	6 ± 2
PT3: $[MAT^+ - H_{amino}^+]$ + HDCA	0	0	4 ± 2	15 ± 4	20 ± 4	19 ± 4	20 ± 4
ion-pair breaking	0	0	0	10 ± 3	35 ± 5	84 ± 4	86 ± 3
fragmentation of MAT$^+$	0	0	0	0	5 ± 2	27 ± 4	34 ± 5
fragmentation of DCA$^-$	0	0	0	2 ± 1	10 ± 3	14 ± 3	17 ± 4

^{a}Percent probabilities and uncertainties were calculated on the basis of 100 trajectories for each condition. Some trajectories have both PT and ion-pair breaking or fragmentation simultaneously or sequentially.

level of theory from 1000 to 8000 K with an interval of 1000 K, each of which was propagated for 1 ps. No dissociation of the MAT$^+$ or the DCA$^-$ moiety was observed at 1000 and 2000 K; less than 30% of the total trajectories were dissociative in the temperature range of 3000−4000 K; on the other hand, almost all trajectories showed fragmentation of MAT$^+$ and/or DCA$^-$ at temperatures above 5000 K. Therefore, five temperatures were chosen from 1000 to 5000 K for running the trajectories at the B3LYP/6-31G(d) level of theory. E_{col} was set to 0.5 eV for trajectories run at 3000 K and below and to 0.1 eV for 4000 K and above (to minimize dissociation). For each initial condition, 100 trajectories were collected.

The trajectory results are summarized in Table 1, where the first column describes the reaction outcomes. Error limits for reaction probabilities are standard statistical uncertainties calculated on the basis of the number of total trajectories and the number of reactive trajectories for the individual paths. No direct reaction was observed between MAT$^+$DCA$^-$ and NO$_2$ at all simulation temperatures. At a temperature below 2000 K, most trajectories maintained an intact-ion-pair structure, but ion-pair breaking increases dramatically starting at 3000 K and is accompanied with fragmentation of the MAT$^+$ and DCA$^-$ moieties via both direct and sequential mechanisms. Except for thermal decomposition, the only reaction observed corresponds to intra-ion-pair PT that occurs via three pathways: the first pathway (PT1) is the transfer of C5−H to a N-terminal of DCA$^-$, forming $[MAT^+ - H_{C5}^+]$ and HDCA; the second pathway (PT2) transfers C5−H to the central N of DCA$^-$, forming $[MAT^+ - H_{C5}^+]$ + HN(CN)$_2$; and the last pathway (PT3) transfers a proton from 4-NH$_2$ to a terminal N of DCA$^-$, forming $[MAT^+ - H_{amino}^+]$ + HDCA. The trajectories of PT2 and PT3 were mostly reversible and returned to the conventional MAT$^+$DCA$^-$ structure before the end of the simulations.

As aforementioned, the trajectory temperatures were much higher than the experimental temperature. As a result, some trajectories may find reaction paths with barriers too high to be of relevance to the IL chemistry at ambient conditions. The point is that with enough trajectories, all of the important collision orientations and reaction paths can be identified, including those that control reactions under the conditions of interest. To determine whether or not the three PT reactions are able to contribute to the experimental reactivity, their relaxed reaction PESs were constructed at the B3LYP/6-311++G(d,p) level of theory. In relaxed PES scans, the bond length ($rH^*−N^*$) that corresponds to respective PT reaction coordinates was varied from 3.0 to 1.1 Å at an interval of 0.025 Å, and all the other bond lengths and bond angles were optimized at each point of the PES. Figure 1 depicts a relaxed PES scan and an IRC scan for the PT1 pathway, in which we have calculated the changes of electronic energy throughout the reaction coordinate. Both the
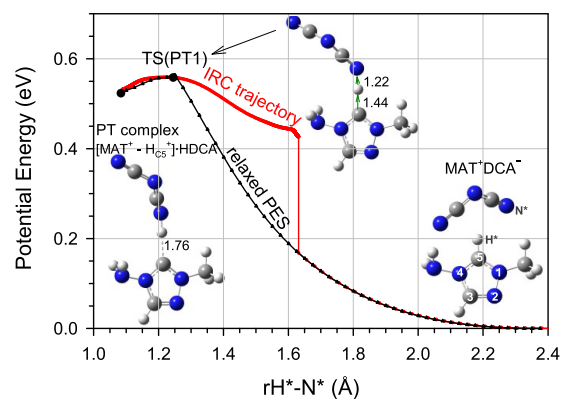

Figure 1. Relaxed PES scan and IRC trajectory for intra-ion-pair proton transfer in MAT$^+$DCA$^-$, calculated at the B3LYP/6-311++G(d,p) level of theory.

IRC and the relaxed PES verified the formation of a stable hydrogen-bonded product complex $[MAT^+ - H_{C5}^+]$·HDCA. The energy of $[MAT^+ - H_{C5}^+]$·HDCA is higher than that of the MAT$^+$DCA$^-$ ion pair by 0.53 eV. Its dissociation energy to separated $[MAT^+ - H_{C5}^+]$ and HDCA is 0.56 eV. Structures of the complex, the TS, and the products found on the PES were then fully optimized, and ZPEs and thermal corrections were added to their energetics. The optimized structures and reaction enthalpies (ΔH) and changes of free energy (ΔG) are given in Table 2. Note that the electronic energy of TS(PT1) is only 0.03 eV above $[MAT^+ - H_{C5}^+]$·HDCA; on the other hand, one vibrational mode that corresponds to the reaction coordinate was removed from TS(PT1) and TS(PT1) also has a highly positive entropy gain ($T\Delta S = 0.12$ eV at 298 K). As a consequence, ΔH and ΔG of TS(PT1) are actually less than $[MAT^+ - H_{C5}^+]$·HDCA, i.e., the reaction surface is constantly increasing from reactant to product on the H and G surfaces.

In contrast to PT1, the PESs for PT2 and PT3 are completely repulsive with no chemically significant interactions between the proton-transferred products. Efforts were made to optimize proton-transferred complexes of $[MAT^+ - H_{C5}^+]$·HN(CN)$_2$ and $[MAT^+ - H_{amino}^+]$·HDCA, but all of the various starting geometries bounced off the repulsive surfaces and transferred the proton back to $[MAT^+ - H_{C5}^+]$. These findings are consistent with reversible PT2 and PT3 observed in the trajectories.

The major findings from the trajectories and PESs of MAT$^+$DCA$^-$ + NO$_2$ are as follows: (1) PT1 is the most energetically favorable and dynamically feasible process, which produces a stable $[MAT^+ - H_{C5}^+]$·HDCA complex as well as separate $[MAT^+ - H_{C5}^+]$ and HDCA that are in equilibrium with MAT$^+$DCA$^-$; (2) because of the repulsive potential

Table 2. Intra-Ion-Pair PT and Ion Pair Breaking Calculated at 298 K Using the B3LYP/6-311++G(d,p) Level of Theory
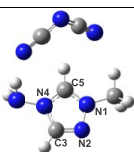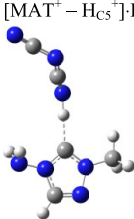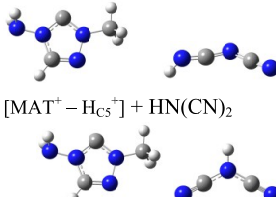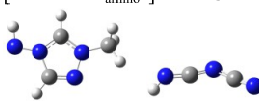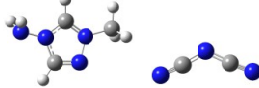
MAT⁺DCA⁻		Products	ΔH (eV)	ΔG (eV)	ΔH(TS) (eV)	ΔG(TS) (eV)
	$\xrightarrow{PT1}$	$[MAT^+ - H_{C5}^+]\cdot HDCA$	0.47	0.33	0.41	0.30
		and $[MAT^+ - H_{C5}^+] + HDCA$	0.99	0.51	—	—
	$\xrightarrow{PT2}$	$[MAT^+ - H_{C5}^+] + HN(CN)_2$	1.34	0.84	—	—
	$\xrightarrow{PT3}$	$[MAT^+ - H_{amino}^+] + HDCA$	1.34	0.86	—	—
	$\rightarrow$	$MAT^+ + DCA^-$	3.97	3.49	—	—

Table 3. Trajectory Reaction Probabilities (%) for HDCA + NO₂ at Various Conditions[a]

temperature (K)	3000	4000		5000			6000		
E_{col} (eV)	0.5	0.5	1.5	0.5	1.0	1.5	0.5	1.0	1.5
HNC(−ONO)NCN	1 ± 1	2 ± 1	3 ± 2	2 ± 1	5 ± 2	6 ± 2	2 ± 1	6 ± 2	8 ± 3
HNCNC(−ONO)N	0	0	1 ± 1	0	1 ± 1	0	1 ± 1	1 ± 1	1 ± 1
DCA + HONO	1 ± 1	4 ± 2	3 ± 2	2 ± 1	4 ± 2	3 ± 2	11 ± 3	10 ± 3	10 ± 3
DCA + O−NH−O	0	1 ± 1	0	1 ± 1	0	0	0	2 ± 1	0
HDCA diss.	0	0	1 ± 1	4 ± 2	3 ± 2	2 ± 1	6 ± 2	11 ± 3	17 ± 4
NO₂ diss.	0	0	1 ± 1	1 ± 1	2 ± 1	0	11 ± 3	11 ± 3	8 ± 3

[a]Percent probabilities and uncertainties were calculated on the basis of 100 trajectories for each condition.

surfaces for PT2 and PT3, any $[MAT^+ - H_{amino}^+]$ and $HN(CN)_2$ products, if formed, would recombine to MAT^+DCA^-; (3) NO_2 is not directly reactive toward MAT^+DCA^-, at least not to an extent that would make it the dominant primary process. These findings thus prompted us to investigate the reactions of NO_2 with neutral $[MAT^+ - H_{C5}^+]$ and HDCA molecules.

3.2. HDCA + NO₂. A batch of 100 trajectories was computed for each of the initial conditions as described in Table 3, and the results were sorted by reaction pathways and products. One common pathway corresponds to the formation of a HNC-(−ONO)NCN complex. The probability of this product channel increases at higher temperatures and E_{col}. It accounts for a percentage yield of up to 3% at 4000 K and increases to 8% at 6000 K. A large fraction of the HNC(−ONO)NCN trajectories are followed by consecutive elimination of NO and NCN. Figure 2a demonstrates a representative trajectory for this pathway. The figure shows the changes in potential energy (PE), reactant E_{col} (before collision), and product recoil energy (E_{recoil}, after the collision) and the variation of various bond

lengths during the trajectory. The large and abrupt changes in PE, E_{col}, and E_{recoil} coincide with the collision instant and the formation and the dissociation of HNC(−ONO)NCN, whereas the high-frequency oscillations in energies reflect the vibrations (including ZPE) of reactants and products. The reaction time depends on the simulation temperature and E_{col}, but three numbers are relevant. The time between the start of the trajectory and the onset of complex formation is ~140 fs (indicated by the change in rC2−ONO), the time for the NO elimination of the complex is 280 fs (indicated by the change in rO−NO), and the time for dissociation of HNC(O)NCN to HNCO (isocyanic acid) + NCN is 450 fs (see the change in rC2−N3). In addition to sequential elimination, a few trajectories revealed complex formation and elimination of NO and NCN simultaneously.

A less common pathway leads to the formation of a HNCNC(−ONO)N complex. This product channel accounts for at most 1% at higher temperatures. HNCNC(−ONO)N may eliminate NO and NCO, as exemplified in Figure 2b, where the dissociation, HNCNC(−ONO)N → HNCN + NCO + NO,
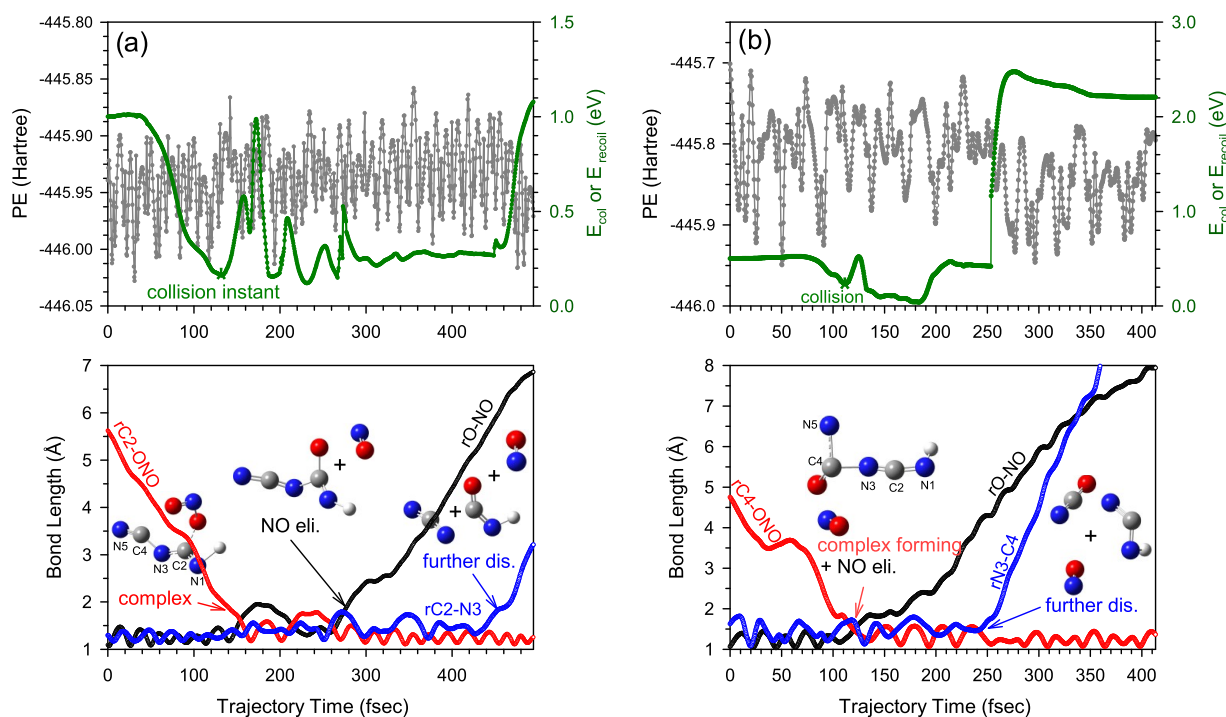
Figure 2. Representative trajectories for the reaction of HDCA with NO_2, showing the formation of (a) $HNC(-ONO)NCN$ at 5000 K and $E_{col} = 1.0$ eV and (b) $HNCNC(-ONO)N$ at 6000 K and $E_{col} = 0.5$ eV. Each top frame shows the changes of potential energy (left axis) and the changes of E_{col} before collision and E_{recoil} after the collision (right axis, green lines). Various bond lengths during the trajectory are shown in the corresponding bottom frames. The inset snapshots illustrate complex formation followed by elimination of NO and NCN/NCO. Videos of the trajectories are available in the Supporting Information.

yields a large amount of energy in product E_{recoil}. The remaining reactive trajectories could be characterized as HT from HDCA to NO_2, producing nitrous acid HNO_2 (in a trans-conformation, a major product) and iminobis(oxy) $O-NH-O$ (a minor product). The possibility of having PT between HDCA and NO_2 can be ruled out because of the 7.55 eV endothermicity and of the Coulomb barrier against charge separation. At 6000 K, thermal decomposition of the reactants becomes severe, which impaired the bimolecular reaction between HDCA and NO_2.

Structures of the complexes and TSs along these pathways were calculated at the B3LYP/6-311++ G(d,p) level of theory, and the results are summarized in Figure 3. We also explored the reactions that might be initiated at various other collision orientations in addition to those found in the trajectory calculations, and their TSs and products are included in Figure 3. It is surprising that the trajectory-predicted pathways of $HNC(-ONO)NCN$ and $HNCNC(-ONO)N$ intermediates do not represent the minimum-energy complex-forming mechanisms on the PES. On the other hand, the two low-energy complex-forming pathways in Figure 3, i.e., reactants → TS2 → $HNC(-NO_2)NCN$ and reactants → TS4 → $HNCNC-(-NO_2)N$ were not observed in direct dynamics at all.

To unravel the above discrepancies between the PES and the direct dynamics, we have utilized the RRKM theory to examine the changes in the reaction kinetics of crossing various TSs in Figure 3 under different reaction conditions. In the first set of RRKM modeling effort (not included here), we included all of the pathways depicted in Figure 3. In this case, we found that the HT channel overwhelmingly dominated under all conditions, with its rate constant increasing from 10^6 s^{-1} at 0.1 eV to 10^9 s^{-1} at 1.5 eV (both at 1000 K). This is in contrast to the trajectory

results where the HT trajectories accounted for at most half of the total reaction probability.

To look into the relative formation efficiencies of the various complexes identified in Figure 3, we did a second set of RRKM calculations where HT was deliberately excluded. The results of the second set are summarized in Table 4. It appears that at 2000 and 3000 K the total rate constant k for complex formation slightly decreases when E_{col} increases from 0.1 to 1.0 eV and then bounces back up at 1.5 eV, albeit all of the product channels are endothermic. The counterintuitive dipping of k with increasing E_{col} can be rationalized by the competition between $T \rightarrow V$ (translational-to-vibrational energy transfer), which helps overcome the reaction barrier and $T \rightarrow R$ (translational-to-rotational energy transfer) that is required by angular momentum conservation and increases at high E_{col} due to the increased orbital angular momentum (i.e., average angular momentum quantum number $J = 112$ at 0.1 eV, 250 at 0.5 eV, 350 at 1.0 eV, and 420 at 1.5 eV). It is likely that the increase in $T \rightarrow V$ at 0.5 and 1.0 eV is not sufficient to compensate for $T \rightarrow R$ at these E_{col}.

But the most striking finding from the comparison between the dynamics simulations and the second set of RRKM modeling results is that the complex formation between HDCA and NO_2 is highly nonstatistical. According to the RRKM product branching ratios (calculated by the ratios of individual unimolecular rates), the dominant complexes should correspond to the nitro complexes, $HNC(-NO_2)NCN$ and $HNCNC(-NO_2)N$, at medium temperatures and the nitrite complex, $HNCNC(-ONO)N$, at higher temperatures, whereas the trajectory-favored complex, $HNC(-ONO)NCN$, represents a low-probability pathway. The origin for the nonstatistical reaction of HDCA with NO_2 is not completely understood. But some factors may have contributed to the nonstatistical
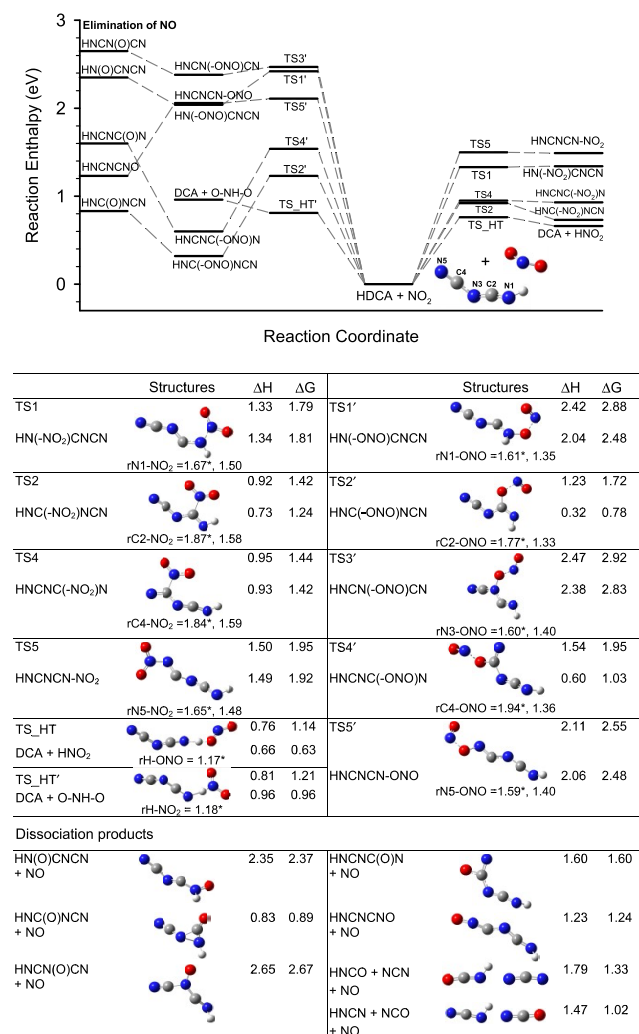
Figure 3 (PES for HDCA + NO$_2$)

Reaction Enthalpy (eV) — Reaction Coordinate

Elimination of NO

Top-level labels: HNCN(O)CN, HN(O)CNCN, HNCN(-ONO)CN, TS3', HNCNCN-ONO, TS1', HN(-ONO)CNCN, TS5', HNCNC(O)N, HNCNCNO, TS5, TS1, HN(-NO2)CNCN, HNC(O)N, HNCNCN-NO2, TS4', TS2', HN(-NO2)CNCN, HNC(-ONO)NCN, HNCN(O)CN, DCA + O-NH-O, TS_HT', HNCNC(-ONO)N, HNC(-ONO)NCN, TS2, TS4, TS_HT, DCA + HNO2, HNCNC(-NO2)N, HNC(-ONO)NCN, HDCA + NO2

Structures table:

Structures	ΔH	ΔG	Structures	ΔH	ΔG
TS1	1.33	1.79	TS1'	2.42	2.88
HN(−NO2)CNCN	1.34	1.81	HN(−ONO)CNCN	2.04	2.48
rN1-NO2 =1.67*, 1.50			rN1-ONO =1.61*, 1.35		
TS2	0.92	1.42	TS2'	1.23	1.72
HNC(−NO2)NCN	0.73	1.24	HNC(−ONO)NCN	0.32	0.78
rC2-NO2 =1.87*, 1.58			rC2-ONO =1.77*, 1.33		
TS4	0.95	1.44	TS3'	2.47	2.92
HNCNC(−NO2)N	0.93	1.42	HNCN(−ONO)CN	2.38	2.83
rC4-NO2 =1.84*, 1.59			rN3-ONO =1.60*, 1.40		
TS5	1.50	1.95	TS4'	1.54	1.95
HNCNCN-NO2	1.49	1.92	HNCNC(−ONO)N	0.60	1.03
rN5-NO2 =1.65*, 1.48			rC4-ONO =1.94*, 1.36		
TS_HT	0.76	1.14	TS5'	2.11	2.55
DCA + HNO2	0.66	0.63			
rH-ONO = 1.17*					
TS_HT'	0.81	1.21	HNCNCN-ONO	2.06	2.48
DCA + O-NH-O	0.96	0.96	rN5-ONO =1.59*, 1.40		
rH-NO2 = 1.18*					
Dissociation products					
HN(O)CNCN + NO	2.35	2.37	HNCNC(O)N + NO	1.60	1.60
HNC(O)NCN + NO	0.83	0.89	HNCNCNO + NO	1.23	1.24
HNCN(O)CN + NO	2.65	2.67	HNCO + NCN + NO	1.79	1.33
			HNCN + NCO + NO	1.47	1.02

Figure 3. PES for HDCA + NO$_2$. Reaction enthalpies and changes of free energy (eV, including ZPE and thermal corrections at 298 K) were calculated at the B3LYP/6-311++G(d,p) level of theory. The critical bond lengths are shown in angstrom and the values for TSs are indicted by asterisks.

Table 4. RRKM Rate Constants and Branching Ratios for Various Complex Formations in the Reaction of HDCA + NO$_2$

temperature (K)	1000				2000				3000			
E_{col} (eV)	0.1	0.5	1.0	1.5	0.1	0.5	1.0	1.5	0.1	0.5	1.0	1.5
k (s^{-1})	3.4×10^2	6.4×10^2	1.3×10^3	4.9×10^3	5.2×10^6	3.7×10^6	3.6×10^6	5.2×10^6	8.0×10^7	6.6×10^7	6.4×10^7	7.1×10^7
TS1 → HN(−NO2)CNCN	none		0.07	0.56	0.04	0.09	0.22	0.30	0.09	0.10	0.15	0.19
TS2 → HNC(−NO2)NCN	0.41	0.33	0.25	0.08	0.25	0.22	0.15	0.07	0.13	0.11	0.08	0.05
TS4 → HNCNC(−NO2)N	0.59	0.67	0.68	0.26	0.59	0.53	0.37	0.29	0.25	0.20	0.15	0.13
TS5 → HNCNCN−NO2	none			0.10	0.01	0.04	0.11	0.20	0.06	0.07	0.12	0.17
TS1' → HN(−ONO)CNCN	none				0.05	0.04	0.02	0.01	0.08	0.06	0.04	0.02
TS2' → HNC(−ONO)NCN	none											
TS3' → HNCN(−ONO)CN	none				0.05	0.09	0.13	0.12	0.39	0.44	0.45	0.41
TS4' → HNCNC(−ONO)N	none							0.01	0.00	0.01	0.02	0.03
TS5' → HNCNCN−ONO	none											

behavior, which include (1) rapid decomposition of NO$_2$-bonded intermediates to reactants (due to their shallow product potential wells, see more discussions below), which results in nonreactivity as a net consequence, and (2) nonstatistical collisional activation, where the attack of NO$_2$ at HDCA may create a "hot spot" and intramolecular vibrational redistribution, is not sufficiently rapid to produce RRKM dynamics. In our studies of thermal decomposition vs. collisional activation and dissociation of 1,5-dinitrobiuret,[14,17] thermal/random and collisional/nonrandom excitations were found to produce dramatically different effects on the reaction dynamics of hypergolic molecules.

3.3. DCA⁻ + NO$_2$. To probe the origin of the no direct reactivity of NO$_2$ with MAT⁺DCA⁻ in the trajectory simulations as well as to compare the NO$_2$ reactivity with HDCA versus DCA⁻, we carried out trajectory simulations for DCA⁻ + NO$_2$ at temperatures of 1500, 2000, 3000, 4000, 5000, and 6000 K and E_{col} of 0.1, 0.5, and 1.0 eV. A batch of 60−100 trajectories was collected for each combination of temperature and E_{col}. Few reactive trajectories were observed, most of which involved short-lived nitro and nitrite complexes with structures of

NCNCN−NO$_2^-$, NCNC(−NO$_2$)N$^-$, and NCNC(−ONO)-N$^-$. The probabilities for forming these complexes varied from 1 to 3%. Figure 4 compares the formation of NCNCN−NO$_2^-$ at
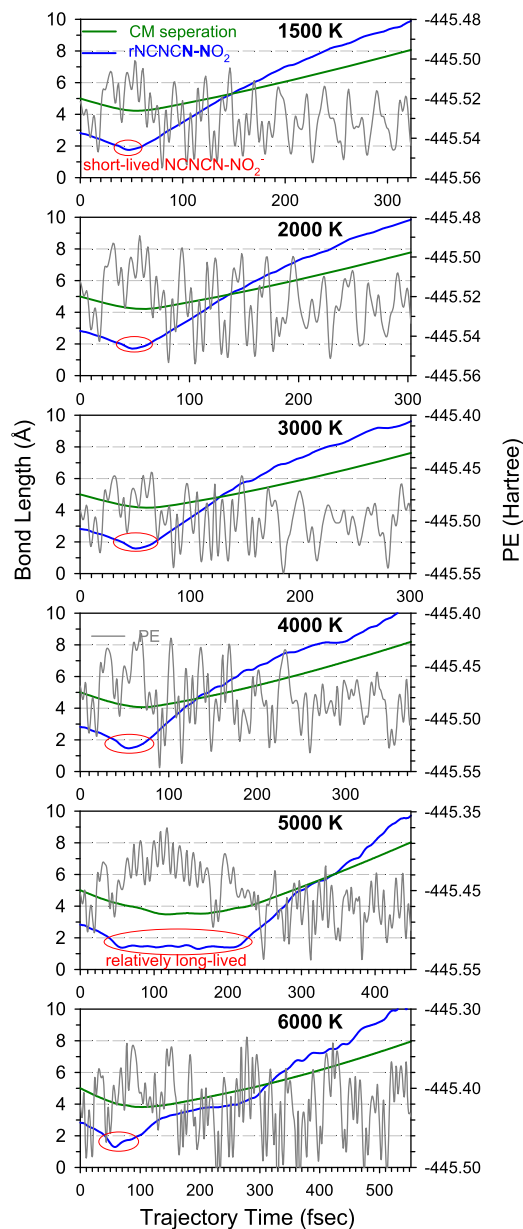

Figure 4. Formation of transient NCNCN−NO$_2^-$ in the trajectories of DCA$^-$ + NO$_2$, simulated at E_{col} = 0.5 eV and various temperatures.

different temperatures and E_{col} = 0.5 eV. The lifetime of NCNCN−NO$_2^-$ increases with increasing temperature and reaches a maximum at 5000 K, before decreasing substantially at 6000 K. In all of the trajectories, the formation of NCNCN−NO$_2^-$ is accompanied by an increase in the PE, which is most obvious at 5000 K. This indicates that the formation of NCNCN−NO$_2^-$ is endothermic and enhanced by E_{vib}.

To probe the transient nature of these complexes, their PESs were mapped out at the B3LYP/6-311++ G(d,p) level of theory in Figure 5. The right half of the figure describes the formation of nitro adducts NCNCN−NO$_2^-$ and NCNC(−NO$_2$)N$^-$. Both NCNCN−NO$_2^-$ and NCNC(−NO$_2$)N$^-$ bear shallow potential wells; in fact, after ZPEs and thermal corrections are accounted for, the two barriers, TS6 and TS7, fall below the products and
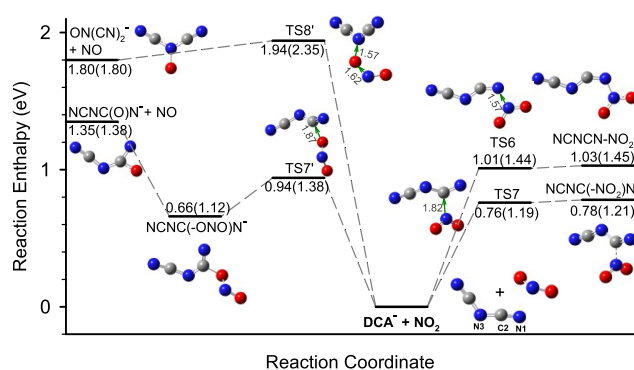

Figure 5. PES for DCA$^-$ + NO$_2$. Reaction enthalpies (eV) and changes of free energy (eV, in parentheses) were calculated at the B3LYP/6-311++G(d,p) level of theory, including ZPE and thermal corrections at 298 K. Vibrational modes corresponding to TS imaginary frequencies are indicated by displacement vectors.

the product potential wells for NCNCN−NO$_2^-$ and NCNC-(−NO$_2$)N$^-$ vanish as a result. Such PES profiles indicate very weak interactions (if any) within NCNCN−NO$_2^-$ and NCNC-(−NO$_2$)N$^-$, and render their decomposition back to reactants readily. We tried to locate a nitroamine complex between NO$_2$ and the central N of DCA$^-$. The resulting PES was found to be more repulsive. The potential is larger than 1.0 eV when the NO$_2$ approaches the central N of DCA$^-$ within 1.6 Å and increases to 2.0 eV when the distance decreases to 1.3 Å.

The left half of Figure 5 depicts the PES for the formation of nitrites via the attack of an O atom of NO$_2$ at DCA$^-$. No stable complex was found when O attacks the terminal N of DCA$^-$. The attack at the central N of DCA$^-$ results in O atom abstraction and produces ON(CN)$_2^-$ + NO, but the associated reaction enthalpy (1.80 eV) and the activation barrier (1.94 eV) make this reaction less important. The attack at the C atoms of DCA$^-$ results in the formation of NCNC(−ONO)N$^-$. As observed in the trajectories, NCNC(−ONO)N$^-$ dissociates to NCNC(O)N$^-$ + NO with a dissociation energy of 0.69 eV (with respect to NCNC(−ONO)N$^-$). The fragments may further dissociate to NCN$^-$ + NCO + NO (2.06 eV with respect to NCNC(−ONO)N$^-$) or NCN + NCO$^-$ + NO (2.43 eV).

The reactions of NO$_2$ with HDCA and DCA$^-$ share some common features in that the N and O atoms of NO$_2$ may bond to various atoms in HDCA and DCA$^-$. For both HDCA + NO$_2$ and DCA$^-$ + NO$_2$, their nitro complexes have no other product exit channels and can only decompose back to starting reactants at high temperatures and high E_{col}; their ONO-bonded complexes (nitrites), on the other hand, may eliminate NO and other fragments that lead to real end-products. In this sense, the nitrite complexes, ONO-HDCA and ONO-DCA$^-$, have higher formation yields than what a statistical mechanism would predict. The different trajectory yields between ONO-HDCA and ONO-DCA$^-$ may be rationalized by their potential well depths and NO elimination energies. The higher reaction efficiency for HDCA + NO$_2$ → HNC(−ONO)NCN could be attributed to the combination of a deep potential well for HNC(−ONO)NCN (the potential well = ΔH(HNC(−ONO)-NCN) − ΔH(TS2′) = −0.91 eV) that blocks TS2′ re-crossing and a low NO-elimination energy (the dissociation energy = ΔH(HNC(O)NCN) + ΔH(NO) − ΔH(HNC(−ONO)-NCN) = 0.51 eV) that facilitates its dissociation. For comparison, the potential well for NCNC(−ONO)N$^-$ = ΔH(NCNC(−ONO)N$^-$) − ΔH(TS7′) is only −0.28 eV, and

Table 5. Trajectory Reaction Probabilities (%) for $[MAT^+ - H_{C5}^+]$ + NO$_2$ at Various Conditions[a]

temperature (K)	300	1000	2000	3000		4000
E_{col} (eV)	0.5	0.5	0.5	0.5	1.0	0.5
5-O-MAT + NO	0	1 ± 1	2 ± 1	3 ± 1	5 ± 2	2 ± 1
5-O$_2$N-MAT (short-lived)	0	0	1 ± 1	1 ± 1	0	1 ± 1
HT: $[MAT^+ - H_2^+]$ + HNO$_2$	0	0	2 ± 1	4 ± 2	4 ± 2	5 ± 2
HT: $[MAT^+ - H_2^+]$ + O−NH−O	0	0	0	0	0	2 ± 1
$[MAT^+ - H_{C5}^+]$ diss.	0	0	1 ± 1	18 ± 4	19	52 ± 5

[a]Percent probabilities and uncertainties were calculated on the basis of 100 trajectories for each condition.

its NO-elimination energy = $\Delta H(NCNC(O)N^-) + \Delta H(NO) - \Delta H(NCNC(-ONO)N^-)$ is higher at 0.69 eV.

3.4. $[MAT^+ - H_{C5}^+]$ + NO$_2$. Collisions of $[MAT^+ - H_{C5}^+]$ with NO$_2$ were simulated at temperatures ranging from 300 to 4000 K and E_{col} from 0.5 to 1.0 eV. Besides the decomposition of $[MAT^+ - H_{C5}^+]$ at high temperatures, the reactive trajectories could be grouped into three types as reported in Table 5. The first type is O-atom abstraction by C5 of $[MAT^+ - H_{C5}^+]$, producing 4-amino-2-methyl-2,4-dihydro-3H-1,2,4-triazo-3-one (5-O-MAT) + NO. This pathway steadily increases with increasing temperature and E_{col} (until at 4000 K when the thermal decomposition of $[MAT^+ - H_{C5}^+]$ inhibits its reaction with NO$_2$). A typical O-atom abstraction trajectory is illustrated in Figure 6. Figure 6a plots system PE, and Figure 6b tracks reactant E_{col} and product E_{recoil} throughout the trajectory. Bond lengths plotted in Figure 6c correspond to various bond dissociation and formation processes. Here again, oscillations in the potential and translational energies are due to molecular vibrations and intermolecular motions. In this trajectory, $[MAT^+ - H_{C5}^+]$ and NO$_2$ begin to interact at 120 fs, as indicated by the onset of E_{col} decrease at this point. The length of time from the beginning of strong interaction to the point when the O-atom is abstracted is 240 fs, during which the repulsive potential converts most of the E_{col} to a combination of PE and internal energy. As a result, E_{col} drops from the initial 0.5 to 0.05 eV. O-atom abstraction is accompanied by the conversion of a fraction of PE (0.08 hartree or 2.2 eV) back to product E_{recoil}, E_{vib}, and E_{rot}, of which 0.35 eV goes to E_{recoil} (so that products have momenta to separate from each other), and the remaining is partitioned into E_{vib} and E_{rot}.

To explore explicit solvent effects in the condensed-phase ILs, the trajectory in Figure 6 was repeated under the same conditions but using the SMD-GIL model. The solvation shell that simulated the effects of the MAT$^+$DCA$^-$ IL surrounding the reaction system was defined as ε (static dielectric constant of the solvent) = 11.5, n^2 (dynamic dielectric constant of the solvent) = 2.0449, α (H bond acidity) = 0.229, β (H bond basicity) = 0.265, γ (surface tension at interface) = 61.24, φ (carbon aromaticity) = 0.2308, and ψ (electronegative halogenicity) = 0.0000.[43] The SMD-GIL-calculated results are presented by the gray plots in Figure 6, so that a direct comparison could be made between the gas-phase and IL-solvated trajectories. The two trajectories have followed essentially similar pathways and collision and reaction time scales, with the only difference being that the product E_{recoil} decreases from 0.3 eV in the gas phase to 0.2 eV in the ILs, and as a result, the IL-solvated trajectory has slower product separation.

The second type of reactive trajectories can be characterized as the formation of an aromatic nitro complex 5-O$_2$N-MAT, where the N-atom of NO$_2$ is bonded to the C5 of $[MAT^+ - H_{C5}^+]$. Similar to the trajectories observed for O$_2$N-HDCA and O$_2$N-DCA$^-$, the trajectories for 5-O$_2$N-MAT are short-lived and decay back to reactants before the end of the simulations. The
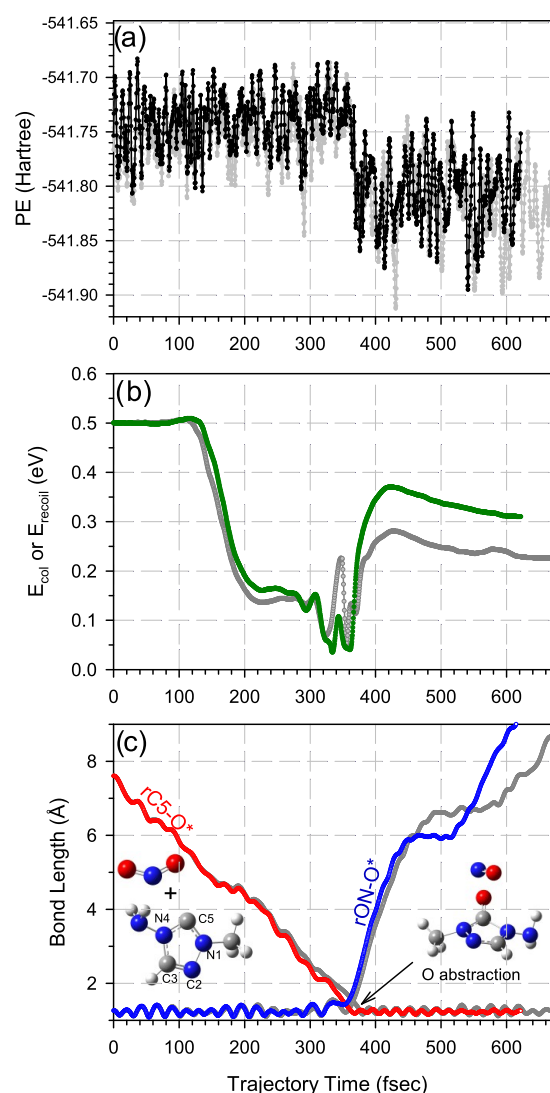

Figure 6. Representative trajectory for the reaction of $[MAT^+ - H_{C5}^+]$ + NO$_2$ → 5-O-MAT + NO calculated at 3000 K and E_{col} = 0.5 eV. The plots show (a) the changes of potential energy, (b) the changes of E_{col} and E_{recoil}, and (c) variations of different bond lengths during the trajectory. The colored plots represent the trajectory results in the gas phase, whereas the gray ones represent the results in the condensed-phase IL (see discussion in the main text). Video of the gas-phase trajectory is available in the Supporting Information.

last type of reactive trajectories represents HT from the NH$_2$ group of $[MAT^+ - H_{C5}^+]$ to NO$_2$, producing cis-HONO (major) or O−NH−O (minor).

The PESs for the three pathways are summarized in Figure 7. The reaction is initiated by the formation of two collision complexes with binding energies of 0.1 eV (with respect to
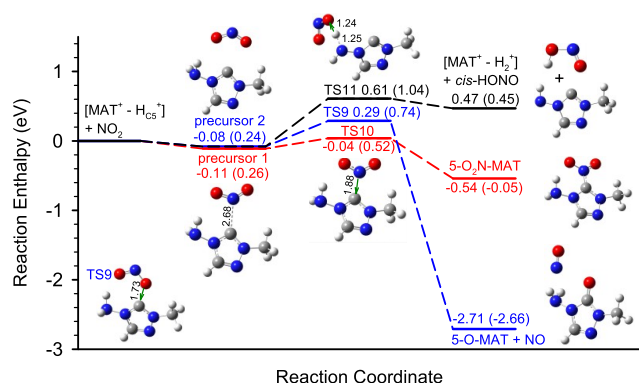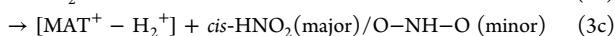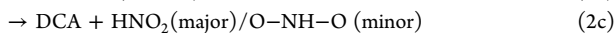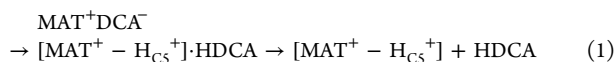
Figure 7. PES for $[MAT^+ - H_{C5}^+] + NO_2$. Reaction enthalpies (eV) and changes of free energy (eV, in parentheses) were calculated at the B3LYP/6-311++G(d,p) level of theory, including ZPE and thermal corrections at 298 K. Vibrational modes corresponding to TS imaginary frequencies are indicated by displacement vectors.

reactants), each of which leads to different pathways. Both O-atom abstraction and formation of 5-O$_2$N-MAT are energetically favorable. The fact that the binding energy of 5-O$_2$N-MAT is only 0.54 eV implies that this complex is best described as an electrostatically bound entity, which is consistent with its transient nature observed in the simulations. Figure 7 shows the HT channel that leads to $[MAT^+ - H_2^+] + cis$-HONO ($\Delta H = 0.47$ eV). The other pair of HT products (not shown), $[MAT^+ - H_2^+] + O-NH-O$, has a higher reaction enthalpy ($\Delta H = 0.73$ eV).

4. COMPARISON WITH EXPERIMENT

4.1. Energetics and Kinetics. The direct dynamics simulations combined with the PES calculations have predicted the following reactions and products

$$MAT^+DCA^-$$
$$\rightarrow [MAT^+ - H_{C5}^+] \cdot HDCA \rightarrow [MAT^+ - H_{C5}^+] + HDCA \quad (1)$$

$$HDCA + NO_2$$
$$\rightarrow HNC(-ONO)NCN \rightarrow HNC(O)NCN + NO \quad (2a)$$
$$\rightarrow HNCNC(-ONO)N \quad (2b)$$
$$\rightarrow DCA + HNO_2(major)/O-NH-O (minor) \quad (2c)$$

$$[MAT^+ - H_{C5}^+] + NO_2$$
$$\rightarrow 5\text{-O-MAT} + NO \quad (3a)$$
$$\rightleftharpoons 5\text{-O}_2\text{N-MAT} \quad (3b)$$
$$\rightarrow [MAT^+ - H_2^+] + cis\text{-HNO}_2(major)/O-NH-O (minor) \quad (3c)$$

$$DCA^- + NO_2$$
$$\rightleftharpoons NCNC(-ONO)N^- \rightarrow NCNC(O)N^- + NO \quad (4a)$$
$$\rightleftharpoons NCNCN - NO_2^- \quad (4b)$$

Among these, the intra-ion-pair PT (reaction 1) dominates as the primary reaction channel and is critical for the subsequent oxidation processes. On the basis of the change of free energy, the equilibrium constant K_{PT} for reaction 1 was estimated to be 1 × 10^{-5} at 298 K and 1.2 at 1000 K. The resulting neutral products HDCA and $[MAT^+ - H_{C5}^+]$ are able to undergo secondary reactions with NO$_2$ (reactions 2 and 3). It could be expected that reactions 1−3 are going on synergistically in that the secondary reactions of HDCA and $[MAT^+ - H_{C5}^+]$ would in turn enhance the slow intra-ion-pair PT in MAT$^+$DCA$^-$. DCA$^-$ may also react with NO$_2$ (reaction 4), albeit it being much less reactive compared to HDCA. One unexpected finding is that the

reactions of NO$_2$ with HDCA and DCA$^-$ are both highly nonstatistical.

Note that Kaiser et al.'s room-temperature experiment[12] had led us to initially look for exothermic reaction pathways for MAT$^+$DCA$^-$ + NO$_2$. However, all of the likely reactions for this system have turned out to be endothermic, as confirmed at different DFT (B3LYP, M06, and M06-2X) and MP2 levels of theory. The more recent levitation experiment has determined that the pseudo-first-order reaction rate of MAT$^+$DCA$^-$ with NO$_2$ is $(0.7-1.0) \times 10^{-4}$ s^{-1} at room temperature.[13] On the basis of thermodynamic transition state theory,[44] which assumes $k(T) = \frac{k_B T}{h} e^{-\Delta G^*(T)/k_B T}$, where k_B is the Boltzmann's constant, T is the reaction temperature, h is the Planck's constant, and $\Delta G^*(T)$ represents the standard free energy of activation, a rate constant of 10^{-4} s^{-1} corresponds to an activation barrier of 1 eV. This activation barrier agrees well with the rate-limiting barriers we have predicted for the MAT$^+$DCA$^-$ + NO$_2$ reaction system.

4.2. Spectral Analysis. To validate whether the theoretical modeling is able to reproduce the spectroscopic measurement results of this system,[12] we have calculated harmonic and anharmonic vibrations (including fundamental frequencies, overtones, and combination bands) and their IR absorptivities and Raman scattering activities for MAT$^+$DCA$^-$ and its reaction products. These calculations were carried out in the condensed-phase IL using the SMD-GIL//B3LYP/6-311++G(d,p) model, which included the ultrafine integration grids, and the solvent descriptor input parameters as described above. The calculated harmonic and anharmonic vibrational frequencies were scaled by an empirical scaling factor of 0.974 and 0.977, respectively. The scaling factors were determined by least-squares fitting of the calculated MAT$^+$DCA$^-$ vibrations to their experimental values. To estimate the relative accuracies of the theoretically predicted spectra, their root-mean-square-deviation (RMSD) was calculated as RMSD $= \sqrt{\frac{1}{m}\sum_{i=1}^{m}(\nu_{i,cal} - \nu_{i,expt})}$, where m is the total number of vibrational frequencies for comparison and $\nu_{i,cal}$ and $\nu_{i,exp}$ are the scaled SMD-GIL//B3LYP/6-311++G(d,p) and experimental frequencies, respectively. RMSD is 30 cm^{-1} for the harmonic spectra of MAT$^+$DCA$^-$ and 20 cm^{-1} for the corresponding anharmonic spectra.

The calculated harmonic and anharmonic spectra of MAT$^+$DCA$^-$ were then convoluted with Gaussian curves with a full width at half-maximum of 30 cm^{-1} for the frequency range below 2450 and 65 cm^{-1} for the frequency range above to best match the experimental linewidths. The resulting IR and Raman spectra were compared with the experimental spectra,[12] as shown in Figures S1 and S2 in the Supporting Information. The assignments of harmonic vibrational peaks in Figure S1 were based on the available experimental data (see Table S1 for details). Apparently, the harmonic IR and Raman spectra of MAT$^+$DCA$^-$ show overall much better matches with the experimental results (Figure S1) than the anharmonic spectra (Figure S2). We have therefore chosen to use the harmonic spectra for spectral analysis and in the identification of products.

Figure 8 presents both IR and Raman spectra for each of the primary and secondary products of reactions 1−4. The spectra of the other (less likely) products are provided in Figure S3 of the Supporting Information. In each spectrum, the peaks that are very close to or overlap with the Kaiser et al.'s experimental MAT$^+$DCA$^-$ vibrations[12] and therefore may be obscured by the MAT$^+$DCA$^-$ peaks in the experiment are labeled in black. The peaks that closely match (within ±30 cm^{-1}) the new product
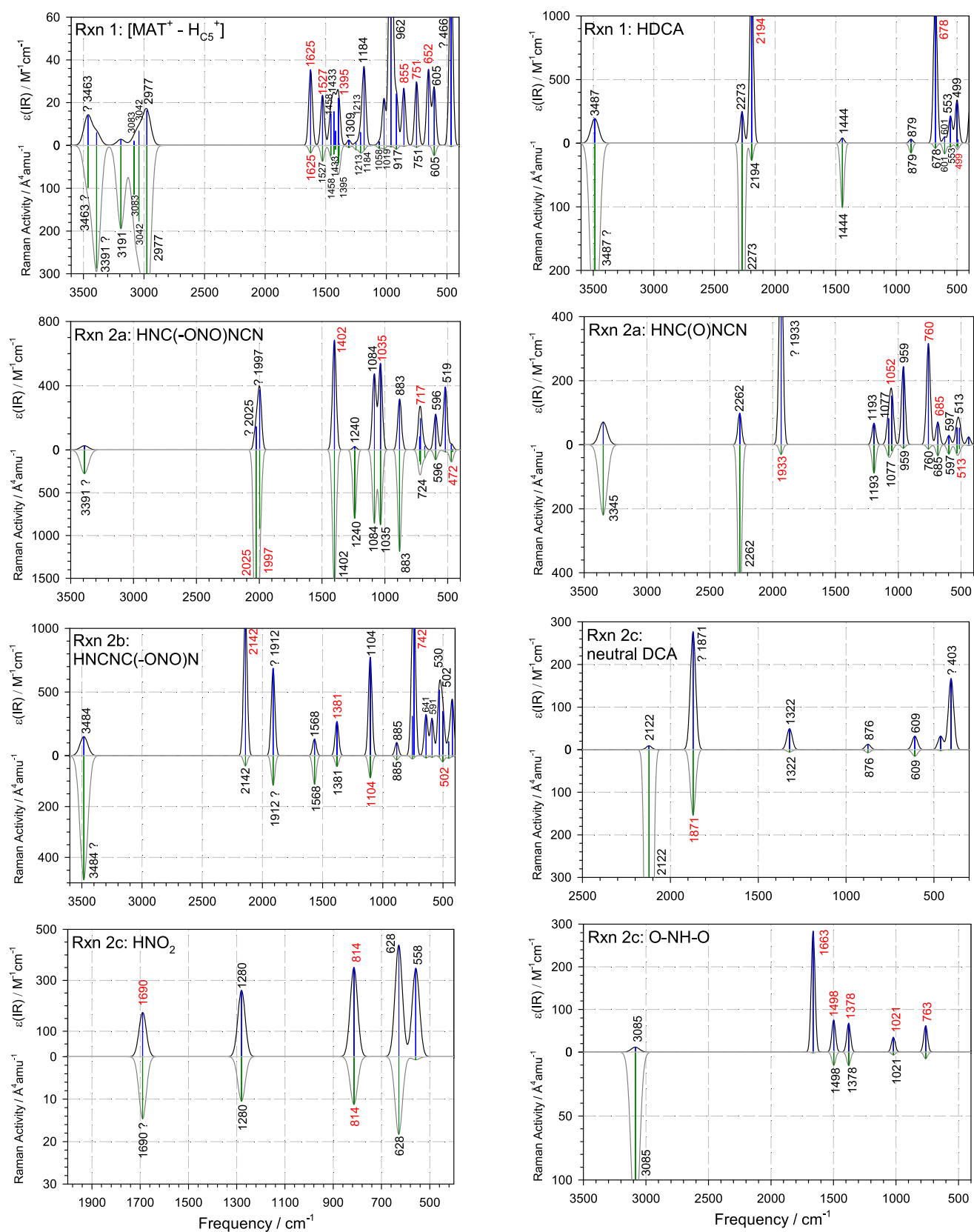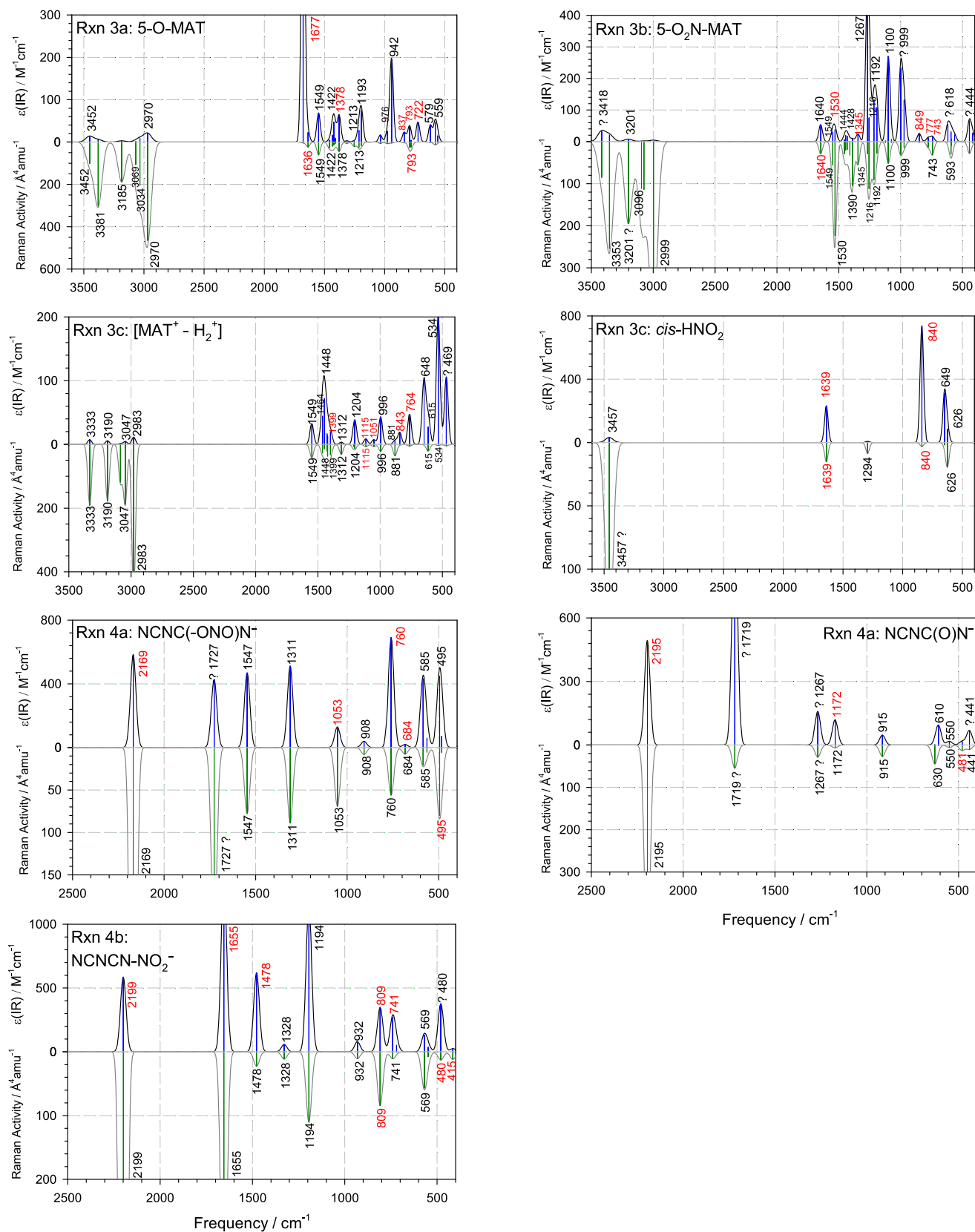
Figure 8. continued

Figure 8. Harmonic IR (top) and Raman (bottom) spectra of trajectory-predicted products simulated at the SMD-GIL//B3LYP/6-311++G(d,p) level of theory. Frequencies were scaled by a factor of 0.974. Red-labeled peaks match experimental products and black-labeled ones are close to MAT⁺DCA⁻ vibrations. Peaks that do not match experimental data are indicated with question marks.

vibrations detected in Kaiser et al.'s experiment are labeled in red. Note that because IR and Raman spectroscopy have

different selection rules and that some vibrational modes may have very close frequency values, it is possible for a calculated

Table 6. Analysis of the New Vibrational Peaks Detected in the Reaction of MAT$^+$DCA$^-$ + NO$_2$

IR (cm^{-1})^a	possible attributions^b	Raman (cm^{-1})^a	possible attributions^b
		409	5-O$_2$N-MAT
		497	HDCA, HNC(−ONO)NCN, HNCNC(−ONO)N, NCNC(−ONO)N$^-$, NCNCN−NO$_2^-$
680	[MAT$^+$ − H$_{C5}^+$], **HDCA**, HNC(O)NCN, NCNC(−ONO)N$^-$		
712	HNC(−ONO)NCN, 5-O-MAT		
757	[MAT$^+$ − H$_{C5}^+$], HNC(O)NCN, **HNCNC(−ONO)N**, O−NH−O, 5-O$_2$N-MAT, **NCNC(−ONO)N$^-$**, NCNCN−NO$_2^-$		
768	**HNC(−O)NCN**, [MAT$^+$ − H$_2^+$]		
778	O−NH−O, 5-O$_2$N-MAT		
815	**HNO$_2$**, 5-O-MAT, NCNCN−NO$_2^-$	813	**HNO$_2$**, 5-O-MAT, **NCNCN−NO$_2^-$**
827	[MAT$^+$ − H$_{C5}^+$], 5-O-MAT, 5-O$_2$N-MAT, [MAT$^+$ − H$_2^+$], *cis*-**HNO$_2$**		
1040	HNC(−ONO)NCN, **HNC(−O)NCN**, O−NH−O, [MAT$^+$ − H$_2^+$], NCNC(−ONO)N$^-$		
1143	HNCNC(−ONO)N	1135	HNCNC(−ONO)N, [MAT$^+$ − H$_2^+$]
1373	[MAT$^+$ − H$_{C5}^+$], **HNC(−ONO)NCN**, HNCNC(−ONO)N, O−NH−O, 5-O-MAT, [MAT$^+$ − H$_2^+$], 5-O$_2$N-MAT		
1497	[MAT$^+$ − H$_{C5}^+$], O−NH−O, 5-O$_2$N-MAT, **NCNCN−NO$_2^-$**		
1613	**[MAT$^+$ − H$_{C5}^+$]**, *cis*-**HNO$_2$**	1611	[MAT$^+$ − H$_{C5}^+$], 5-O-MAT, 5-O$_2$N-MAT, *cis*-**HNO$_2$**
1677	**HNO$_2$, O−NH−O, 5-O-MAT, NCNCN−NO$_2^-$**		
		1782	N$_2$O$_4$, NCNC(−ONO)N$^-$, NCNC(O)N$^-$
		1868	**DCA**
		1960	HNC(O)NCN
		2010	**HNC(−ONO)NCN**
		2071	**HNC(−ONO)NCN**
2177	**HDCA, HNCNC(−ONO)N, NCNC(−ONO)N$^-$, NCNCN−NO$_2^-$**		

^{a}Ref 12. ^{b}The species in bold presents a dominating IR or Raman intensity at the assigned frequency.

frequency value to have a black labeled peak in IR spectrum and a red labeled peak in Raman spectrum (and vice versa). The peaks that cannot match any of the experimentally detected vibrations are indicated with question marks. The origin of these mismatches could be due to the combined uncertainties from the experimental measurements and the theoretical calculations, as exemplified in the comparison of experimental and theoretical spectra of MAT$^+$DCA$^-$ in Figure S1.

The product pair of [MAT$^+$ − H$_{C5}^+$] + HDCA (reaction 1) are among the most probable species that were detected in the experiment. This identification was based on their unique IR peaks of 652 (out-of-plane ring wag), 751 (in-plane ring rock), 855 (CH out-of-plane wag), 1395 (CN stretch), 1527 (NCN antisymmetric stretch), and 1625 cm^{-1} (NH$_2$ bend) for [MAT$^+$ − H$_{C5}^+$] and 678 (HNC bend) and 2194 cm^{-1} (HN−C−NCN antisymmetric stretch) for HDCA. The vibrations of 678 and 2194 cm^{-1} are the two dominating peaks in the IR spectrum of HDCA. In addition, [MAT$^+$ − H$_{C5}^+$] presents a low-intensity Raman peak at 1625 cm^{-1} and HDCA presents a low-intensity Raman peak at 499 cm^{-1}. There are a few question-marked IR and Raman peaks for [MAT$^+$ − H$_{C5}^+$] and HDCA for the frequency range over 3200 cm^{-1}. We found that the uncertainty of the calculated harmonic frequencies increases in this high-frequency range.

The second group of products that were likely captured in the experiment are HNC(−ONO)NCN and its decomposition product HNC(−O)NCN (reaction 2a). HNC(−ONO)NCN displays IR features at 717 (NH out-of-plane wag), 1035 (CN stretch), and 1402 cm^{-1} (CO stretch) and Raman features at 472 (NCN scissors), 1997 (NO stretch and NCN antisymmetric stretch), and 2025 cm^{-1} (NCN antisymmetric stretch and NO stretch). The formation of HNC(−O)NCN was supported by IR peaks at 685 (CNC scissors), 760 (CNC

symmetric stretch), and 1052 cm^{-1} (HNC scissors). Note that the intense IR peaks of HNC(−ONO)NCN at 1997 cm^{-1} (NO stretch) and HNC(−O)NCN at 1933 cm^{-1} (CO stretch) could not be matched with the experimental IR spectra, albeit the vibration of 1933 cm^{-1} was indeed detected in the experimental Raman spectra. Also note that although vibrational frequencies can be predicted theoretically well, vibrational intensities often cannot be.

The formation of HNCNC(−ONO)N (reaction 2b) in the experiment could be verified by several IR peaks at 742 (HNC scissors), 1381 (NCN symmetric stretch), and 2142 cm^{-1} (NCN antisymmetric stretch) and Raman peaks at 502 (OCN scissors) and 1104 cm^{-1} (CO stretch). Similar to HNC-(−ONO)NCN, HNCNC(−ONO)N presents an NO stretch mode at 1912 cm^{-1}, which was not found in the experiment.

The product pair of neutral DCA and HNO$_2$ (reaction 2c) presents the IR and Raman spectra that match the experimental vibrational peaks. Besides sharing many similar vibrations as its anionic counterpart in the reactant MAT$^+$DCA$^-$, neutral DCA shows a strong Raman signal at 1871 cm^{-1} due to an antisymmetric NCN stretch (the same mode shifts to 2168 cm^{-1} in MAT$^+$DCA$^-$). Note that although the 1871 cm^{-1} vibration was calculated to be both IR and Raman strongly active, this mode was missing in the experimental IR measurement. The IR peaks of HNO$_2$ at 814 (N−OH stretch) and 1690 cm^{-1} (NO stretch) and the Raman peak of HNO$_2$ at 814 cm^{-1} closely match the experimental product data. Although O−NH−O is a minor product of reaction 2c based on the dynamics simulations and the reaction PES, its IR spectrum shows nearly all experimentally matching peaks at the frequency range of 500 to 1500 cm^{-1}, including 763 (ONO scissors), 1021 (out-of-lane NH wag), 1378 (ONO symmetric

stretch), 1498 (NH in-plane rock), and 1663 cm^{-1} (ONO antisymmetric stretch).

5-O-MAT of reaction 3a shows a very distinct peak at 1677 cm^{-1} (CO stretch) along with several others of minor intensities. 5-O$_2$N-MAT of reaction 3b, on the other hand, shows only a few small peaks. Therefore, it is difficult to confirm the formation of 5-O$_2$N-MAT in the experiment. A similar scenario is seen for $[MAT^+ - H_2^+]$ (reaction 3c), where all of its peaks are more or less indistinct. Its complementary product *cis*-HNO$_2$, on the other hand, has very strong peaks at 840 (HO–N stretch) and 1639 cm^{-1} (NO stretch). As shown in Figure 8, conventional HNO$_2$ (that is in a trans-conformer, produced from reaction 2c) and *cis*-HNO$_2$ have dramatically different vibrational spectra. Note that *cis*-HNO$_2$ is 0.04 eV higher in energy than conventional HNO$_2$ and has an isomerization barrier of 0.50 eV.

Finally, we have examined the spectra of NCNC(−ONO)N$^-$ (reaction 4a) and NCNCN−NO$_2^-$ (reaction 4b). Both NCNC(−ONO)N$^-$ and its NO-elimination product NCNC-(−O)N$^-$ have shown some IR and Raman peaks. But the most intense IR peak of NCNC(−O)N$^-$ at 1719 cm^{-1} (CN stretch) was not detected in the experiment; we therefore tend to rule out the formation of NCNC(−O)N$^-$ in the experiment. NCNCN−NO$_2^-$ seems the most likely product for DCA$^-$ + NO$_2$ in the experiment, as the spectra of NCNCN−NO$_2^-$ present a progression of high-intensity IR peaks at 741 (NCN scissors), 809 (ONO scissors), 1478 (ONO antisymmetric stretch), 1655 (NCN antisymmetric stretch), and 2199 cm^{-1} (NCN antisymmetric stretch) that match the experimental new product peaks.

Table 6 summarizes all of the new IR and Raman peaks that Kaiser et al. detected in their experimental measurements on MAT$^+$DCA$^-$ + NO$_2$. These are the peaks that can be clearly distinguished from reactant vibrations. Each of these peaks can be attributed to one or more reaction products of reactions 1−4 on the basis of the above spectral analysis. The only experimental product peak for which we were not able to find a definite match is the Raman peak at 1782 cm^{-1}. Note that this frequency is close to (and thus may represent) a Raman-active NO stretch mode in N$_2$O$_4$, which is in equilibrium with NO$_2$. Alternatively, it may be assigned to a combination band of NCNC(−ONO)N$^-$ ($7^1 5^1$) and/or NCNC(O)N$^-$ ($4^1 6^1$).

5. CONCLUSIONS

Direct dynamics trajectories were used to predict the most likely reaction pathways and products of MAT$^+$DCA$^-$ with NO$_2$ at the B3LYP/6-31G(d) level of theory. Analysis of the trajectory outcomes combined with the PES computations for the trajectory-predicted reactions at the B3LYP/6-311++G(d,p) level revealed the dominant intra-ion-pair proton transfer of MAT$^+$DCA$^-$ and the secondary reactions of the proton-transferred HDCA and $[MAT^+ - H_{C5}^+]$ with NO$_2$. The overall good match between the theoretically simulated and experimentally measured reaction kinetics and vibrational spectra of reaction products suggests that our computational modeling has captured the important reaction dynamics for MAT$^+$DCA$^-$ with NO$_2$.

As an additional note, Kaiser et al. recently reported a similar IR and Raman spectroscopic investigation of the reaction of the IL droplet of 1-butyl-3-methyl-imidazolium dicyanamide (BMIM$^+$DCA$^-$) with NO$_2$.[13] We may reasonably assume that the differences between the reaction products of MAT$^+$DCA$^-$ + NO$_2$ and BMIM$^+$DCA$^-$ + NO$_2$ should most likely result from

the different IL cations, MAT$^+$ versus BMIM$^+$, whereas their similarities might be associated with the same DCA$^-$ anion and HDCA molecule reactants. When comparing the product vibrational spectra of BMIM$^+$DCA$^-$ + NO$_2$ versus MAT$^+$DCA$^-$ + NO$_2$, we have indeed found many common vibrational frequencies including the IR peaks of 680, 740, 773, 790, 827, 1041, 1364, 1510, 1624, and 1652 cm^{-1} and the Raman peaks of 410, 491, 820, 1138, 1616, 1869, 1981, and 2038 cm^{-1}. The fact that all of these common vibrational peaks can also be accounted for by the reaction products of HDCA + NO$_2$ and/or DCA$^-$ + NO$_2$ (see Table 6) further supports our results of direct dynamics simulations and product spectral analyses.

Note that the experimental kinetics results of NO$_2$ with MAT$^+$DCA$^-$ and BMIM$^+$DCA$^-$ indicate that the reaction rate constant of MAT$^+$DCA$^-$ is a factor of 20 lower than that of BMIM$^+$DCA$^-$. This implies that, despite their similarities, there exist large differences in the energetics and the dynamics between MAT$^+$DCA$^-$ + NO$_2$ and BMIM$^+$DCA$^-$ + NO$_2$. Rather than speculating, we defer the discussion until we complete the reaction dynamics and PES study for BMIM$^+$DCA$^-$ + NO$_2$, which is currently underway.

■ ASSOCIATED CONTENT

⑤ Supporting Information

The Supporting Information is available free of charge on the ACS Publications website at DOI: 10.1021/acs.jpcb.9b01015.

> IR and Raman spectra of MAT$^+$DCA$^-$ (in comparison with experimental data), HNC(−NO$_2$)NCN, HNCNC-(−NO$_2$)N, NCNC(NO$_2$)N$^-$, and ON(CN)$_2^-$; Cartesian coordinates for the structures in Figures 1, 3, 5, 7, and Table 2 (PDF)
>
> Videos for the trajectories shown in Figures 2 and 6 (MPG)(MPG)(MPG)

■ AUTHOR INFORMATION

Corresponding Author

*E-mail: jianbo.liu@qc.cuny.edu. Tel: 1-718-997-3271.

ORCID ⓘ

Jianbo Liu: 0000-0001-9577-3740

Ghanshyam L. Vaghjiani: 0000-0001-7473-7388

Notes

The authors declare no competing financial interest.

■ REFERENCES

(1) Clark, J. D. *Ignition. An Informal History of Liquid Rocket Propellants*; Rutgers University Press, 1972; p 214.

(2) Gao, Y.; Gao, H.; Piekarski, C.; Shreeve, J. M. Azolium Salts Functionalized with Cyanomethyl, Vinyl, or Propargylsubstituents and Dicyanamide, Dinitramide, Perchlorate and Nitrate Anions. *Eur. J. Inorg. Chem.* **2007**, 4965−4972.

(3) Schneider, S.; Hawkins, T.; Rosander, M.; Vaghjiani, G.; Chambreau, S.; Drake, G. Ionic Liquids as Hypergolic Fuels. *Energy Fuels* **2008**, 22, 2871−2872.

(4) Zhang, Y.; Gao, H.; Joo, Y.-H.; Shreeve, J. M. Ionic Liquids as Hypergolic Fuels. *Angew. Chem., Int. Ed.* **2011**, *50*, 9554−9562.

(5) L. Perez, J. P.; McMahon, B. W.; Schneider, S.; Boatz, J. A.; Hawkins, T. W.; McCrary, P. D.; Beasley, P. A.; Kelley, S. P.; Rogers, R. D.; Anderson, S. L. Exploring the Structure of Nitrogen-Rich Ionic Liquids and Their Binding to the Surface of Oxide-Free Boron Nanoparticles. *J. Phys. Chem. C* **2013**, *117*, 5693−5707.

(6) McCrary, P. D.; Chatel, G.; Alaniz, S. A.; Cojocaru, O. A.; Beasley, P. A.; Flores, L. A.; Kelley, S. P.; Barber, P. S.; Rogers, R. D. Evaluating Ionic Liquids as Hypergolic Fuels: Exploring Reactivity from Molecular Structure. *Energy Fuels* **2014**, *28*, 3460−3473.

(7) Chambreau, S. D.; Schenk, A. C.; Sheppard, A. J.; Yandek, G. R.; Vaghjiani, G. L.; Maciejewski, J.; Koh, C. J.; Golan, A.; Leone, S. R. Thermal Decomposition Mechanism of Alkylimidazolium Ionic Liquids with Cyano-Containing Anions. *J. Phys. Chem. A* **2014**, *118*, 11119−11132.

(8) Liu, J.; Chambreau, S. D.; Vaghjiani, G. L. Dynamics Simulations and Statistical Modeling of Thermal Decomposition of 1-Ethyl-3-Methylimidazolium Dicyanamide and 1-Ethyl-2,3-Dimethylimidazolium Dicyanamide. *J. Phys. Chem. A* **2014**, *118*, 11133−11144.

(9) Nichols, C. M.; Wang, Z.-C.; Yang, Z.; Lineberger, W. C.; Bierbaum, V. M. Experimental and Theoretical Studies of the Reactivity and Thermochemistry of Dicyanamide: N(CN)$_2$. *J. Phys. Chem. A* **2016**, *120*, 992−999.

(10) Chambreau, S. D.; Koh, C. J.; Popolan-Vaida, D. M.; Gallegos, C. J.; Hooper, J. B.; Bedrov, D.; Vaghjiani, G. L.; Leone, S. R. Flow-Tube Investigations of Hypergolic Reactions of a Dicyanamide Ionic Liquid Via Tunable Vacuum Ultraviolet Aerosol Mass Spectrometry. *J. Phys. Chem. A* **2016**, *120*, 8011−8023.

(11) Schmidt, M. W.; Gordon, M. S. Effect of Boron Clusters on the Ignition Reaction of HNO$_3$ and Dicyanamide-Based Ionic Liquids. *J. Phys. Chem. A* **2017**, *121*, 8003−8011.

(12) Brotton, S. J.; Lucas, M.; Chambreau, S. D.; Vaghjiani, G. L.; Yu, J.; Anderson, S. L.; Kaiser, R. I. Spectroscopic Investigation of the Primary Reaction Intermediates in the Oxidation of Levitated Droplets of Energetic Ionic Liquids. *J. Phys. Chem. Lett.* **2017**, *8*, 6053−6059.

(13) Brotton, S. J.; Lucas, M.; Jensen, T. N.; Anderson, S. L.; Kaiser, R. I. Spectroscopic Study on the Intermediates and Reaction Rates in the Oxidation of Levitated Droplets of Energetic Ionic Liquids by Nitrogen Dioxide. *J. Phys. Chem. A* **2018**, *122*, 7351−7377.

(14) Liu, J.; Chambreau, S. D.; Vaghjiani, G. L. Thermal Decomposition of 1,5-Dinitrobiuret (DNB): Direct Dynamics Trajectory Simulations and Statistical Modeling. *J. Phys. Chem. A* **2011**, *115*, 8064−8072.

(15) Liu, J.; Anderson, S. L. Dynamical Control of 'Statistical' Ion-Molecule Reactions. *Int. J. Mass Spectrom.* **2005**, *241*, 173−184.

(16) Chowdhury, A.; Thynell, S. T. Confined Rapid Thermolysis/FTIR/ToF Studies of Imidazolium-Based Ionic Liquids. *Thermochim. Acta* **2006**, *443*, 159−172.

(17) Sun, R.; Siebert, M. R.; Xu, L.; Chambreau, S. D.; Vaghjiani, G. L.; Lischka, H.; Liu, J.; Hase, W. L. Direct Dynamics Simulation of the Activation and Dissociation of 1,5-Dinitrobiuret (HDNB). *J. Phys. Chem. A* **2014**, *118*, 2228−2236.

(18) Ma, X.; Hase, W. L. Perspective: Chemical Dynamics Simulations of Non-Statistical Reaction Dynamics. *Philos. Trans. R. Soc., A* **2017**, *375*, No. 20160204.

(19) Car, R.; Parrinello, M. Unified Approach for Molecular Dynamics and Density Functional Theory. *Phys. Rev. Lett.* **1985**, *55*, 2471−2474.

(20) Baldridge, K. K.; Gordon, M. S.; Steckler, R.; Truhlar, D. G. Ab Initio Reaction Paths and Direct Dynamics Calculations. *J. Phys. Chem.* **1989**, *93*, 5107−5119.

(21) Helgaker, T.; Uggerud, E.; Jensen, H. J. A. Integration of the Classical Equations of Motion on ab Initio Molecular Potential Energy Surfaces Using Gradients and Hessians: Application to Translational Energy Release Upon Fragmentation. *Chem. Phys. Lett.* **1990**, *173*, 145−150.

(22) Bolton, K.; Hase, W. L.; Peslherbe, G. H. Direct Dynamics Simulations of Reactive Systems. *Modern Methods for Multidimensional Dynamics Computations in Chemistry*; World Scientific, 1998; pp 143−189.

(23) Hase, W. L. Advances in Classical Trajectory Methods. Vol.*1*; *Intramolecular and Nonlinear Dynamics*; JAI Press: Greenwich, 1992; p 339.

(24) Bakken, V.; Millam, J. M.; Schlegel, H. B. Ab Initio Classical Trajectories on the Born-Oppenheimer Surface: Updating Methods for Hessian-Based Integrators. *J. Chem. Phys.* **1999**, *111*, 8773−8777.

(25) Döntgen, M.; Przybylski-Freund, M.-D.; Kröger, L. C.; Kopp, W. A.; Ismail, A. E.; Leonhard, K. Automated Discovery of Reaction Pathways, Rate Constants, and Transition States Using Reactive Molecular Dynamics Simulations. *J. Chem. Theory Comput.* **2015**, *11*, 2517−2524.

(26) Martínez-Núñez, E. An Automated Transition State Search Using Classical Trajectories Initialized at Multiple Minima. *Phys. Chem. Chem. Phys.* **2015**, *17*, 14912−14921.

(27) Pratihar, S.; Ma, X.; Homayoon, Z.; Barnes, G. L.; Hase, W. L. Direct Chemical Dynamics Simulations. *J. Am. Chem. Soc.* **2017**, *139*, 3570−3590.

(28) Martínez-Núñez, E. An Automated Method to Find Transition States Using Chemical Dynamics Simulations. *J. Comput. Chem.* **2015**, *36*, 222−234.

(29) Marcus, R. A. Unimolecular Dissociations and Free-Radical Recombination Reactions. *J. Chem. Phys.* **1952**, *20*, 359−364.

(30) Hase, W. L.; Bolton, K.; de Sainte Claire, P.; Duchovic, R. J.; Hu, X.; Komornicki, A.; Li, G.; Lim, K.; Lu, D.; Peslherbe, G. H.; Song, K.; Swamy, K. N.; Vande Linde, S. R.; Varandas, A.; Wang, H.; Wolf, R. J. *Venus 99: A General Chemical Dynamics Computer Program*; Texas Tech University: Lubbock, TX, 1999.

(31) Hu, X.; Hase, W. L.; Pirraglia, T. Vectorization of the General Monte Carlo Classical Trajectory Program Venus. *J. Comput. Chem.* **1991**, *12*, 1014−1024.

(32) Frisch, M. J.; Trucks, G. W.; Schlegel, H. B.; Scuseria, G. E.; Robb, M. A.; Cheeseman, J. R.; Scalmani, G.; Barone, V.; Mennucci, B.; Petersson, G. A. et al. *Gaussian 09*, revision B.01; Gaussian, Inc., 2009.

(33) Kroon, M. C.; Buijs, W.; Peters, C. J.; Witkamp, G.-J. Quantum Chemical Aided Prediction of the Thermal Decomposition Mechanisms and Temperatures of Ionic Liquids. *Thermochim. Acta* **2007**, *465*, 40−47.

(34) Emel'yanenko, V. N.; Verevkin, S. P.; Heintz, A. The Gaseous Enthalpy of Formation of the Ionic Liquid 1-Butyl-3-Methylimidazolium Dicyanamide from Combustion Calorimetry, Vapor Pressure Measurements, and Ab Initio Calculations. *J. Am. Chem. Soc.* **2007**, *129*, 3930−3937.

(35) Verevkin, S. P.; Emel'yanenko, V. N.; Zaitsau, D. H.; Heintz, A.; Muzny, C. D.; Frenkel, M. Thermochemistry of Imidazolium-Based Ionic Liquids: Experiment and First-Principles Calculations. *Phys. Chem. Chem. Phys.* **2010**, *12*, 14994−15000.

(36) Hollóczki, O.; Gerhard, D.; Massone, K.; Szarvas, L.; Németh, B.; Veszprémi, T.; Nyulászi, L. Carbenes in Ionic Liquids. *New J. Chem.* **2010**, *34*, 3004−3009.

(37) Clough, M. T.; Geyer, K.; Hunt, P. A.; Mertes, J.; Welton, T. Thermal Decomposition of Carboxylate Ionic Liquids: Trends and Mechanisms. *Phys. Chem. Chem. Phys.* **2013**, *15*, 20480−20495.

(38) Bacskay, G. B. A Quadratically Convergent Hartree-Fock (QC-SCF) Method. Application to Closed Shell Systems. *Chem. Phys.* **1981**, *61*, 385−404.

(39) Laaksonen, L. *gOpenMol*, version 3.0; Center for Scientific Computing: Espoo, Finland, 2005.

(40) Zheng, J.; Alecu, I. M.; Lynch, B. J.; Zhao, Y.; Truhlar, D. G. *Database of Frequency Scale Factors for Electronic Model Chemistries*, version 2, 2010. http://comp.chem.umn.edu/freqscale/version2.htm.

(41) Zhu, L.; Hase, W. L. *A General RRKM Program (QCPE 644), Quantum Chemistry Program Exchange*; Chemistry Department, University of Indiana: Bloomington, 1993.

(42) Marenich, A. V.; Cramer, C. J.; Truhlar, D. G. Universal Solvation Model Based on Solute Electron Density and on a Continuum Model of the Solvent Defined by the Bulk Dielectric Constant and Atomic Surface Tensions. *J. Phys. Chem. B* **2009**, *113*, 6378−6396.

(43) Bernales, V. S.; Marenich, A. V.; Contreras, R.; Cramer, C. J.; Truhlar, D. G. Quantum Mechanical Continuum Solvation Models for Ionic Liquids. *J. Phys. Chem. B* **2012**, *116*, 9122−9129.

(44) Truhlar, D. G.; Garrett, B. C.; Klippenstein, S. J. Current Status of Transition-State Theory. *J. Phys. Chem.* **1996**, *100*, 12771−12800.